Available online at www.sciencedirect.com

ScienceDirect

Geochimica et Cosmochimica Acta 132 (2014) 16–30

Geochimica et Cosmochimica Acta

www.elsevier.com/locate/gca

Oxidation and mobilization of metallic antimony in aqueous systems with simulated groundwater

A.G. Ilgen [a,*], F. Majs [a], A.J. Barker [a,b], T.A. Douglas [b], T.P. Trainor [a]

[a] *University of Alaska Fairbanks, Department of Chemistry and Biochemistry, 900 Yukon Dr. Rm 194, Fairbanks, AK 99775-6160, United States*
[b] *US Army Corps of Engineers, Cold Regions Research and Engineering Laboratory, Fort Wainwright, AK 99709, United States*

Received 25 April 2013; accepted in revised form 15 January 2014; available online 1 February 2014

Abstract

Antimony (Sb) is a contaminant of concern that can be present in elevated concentrations in shooting range soils due to mobilization from spent lead/antimony bullets. Antimony in shooting range soils has been observed as either metallic Sb(0) or as Sb(V) immobilized by iron (hydr)oxides. The absence of Sb(III) in soils is indicative of rapid Sb(III) oxidation to Sb(V) under surface soil conditions. However, the major controls on antimony oxidation and mobility are poorly understood. To better understand these controls we performed multiple batch experiments under oxic conditions to quantify the oxidation and dissolution of antimony in systems where Sb(0) is oxidized to Sb(III) and further to Sb(V). We also tested how variations in the aqueous matrix composition and the presence of metallic lead (Pb) affect the dissolution, solid phase speciation, and oxidation of antimony. We monitored changes in the aqueous antimony speciation using liquid chromatography inductively coupled plasma mass spectrometry (LC-ICP-MS). To test which solid phases form as a result of Sb(0) oxidation, and therefore potentially limit the mobility of antimony in our studied systems, we characterized the partially oxidized Sb(0) powders by means of extended X-ray absorption fine structure (EXAFS) spectroscopy and powder X-ray diffraction (XRD).

The observed oxidation of Sb(0) to Sb(III) and mobilization to solution is rapid: after 5–15 min of reaction the aqueous antimony concentration reached 50–600 μM. The amount of dissolved antimony and the rate of Sb(III) oxidation to Sb(V) in deionized water is lower than what we measured in the simulated groundwater systems. Sénarmontite (Sb_2O_3), the primary crystalline oxidation product of Sb(0), was detected after one month from the beginning of Sb(0) oxidation. The maximum aqueous Sb(III) concentration is about 30 times larger than the predicted equilibrium concentration with respect to sénarmontite in the initial stages (<65 h) of our experiment. Concentrations reach equilibrium within 146–222 days. The maximum concentration of Sb(V) is controlled by cation availability for the precipitation of an antimonate. In the systems where sodium Na(I) exceeded 20 mM precipitation of mopungite is observed. No crystalline phases were detected in the systems with added lead, and the dissolved Sb(V) concentration is several orders of magnitude higher than would be expected in equilibrium with bindheimite ($Pb_2Sb_2O_7$). The observed solubility of Sb(V) in the systems with Ca(II) is several orders of magnitude larger than the solubility reported for roméite ($Ca_2Sb_2O_7$). The addition of Pb(0) lowered the extent of Sb(0) oxidation due to competitive oxidation or to the coupling of antimony and lead redox reactions. The results from our research can be used to identify substrates that promote precipitation of relatively insoluble antimony compounds in target berm soils and thus prevent the offsite migration of antimony from shooting range target berms.
© 2014 Elsevier Ltd. All rights reserved.

1. INTRODUCTION

The distribution and behavior of antimony (Sb) in the environment has been the topic of an increasing number of studies which are summarized in several recent reviews

* Corresponding author. Present address: Sandia National Laboratories, Geochemistry Department, 1515 Eubank SE Mailstop 0754, Albuquerque, NM 87185-0754, United States. Tel.: +1 5052841393.
E-mail address: agilgen@sandia.gov (A.G. Ilgen).

http://dx.doi.org/10.1016/j.gca.2014.01.019
0016-7037/© 2014 Elsevier Ltd. All rights reserved.

(Wilson et al., 2010; Filella and Williams, 2012; Roper et al., 2012). Studies focused on the mechanisms related to toxic, teratogenic, and carcinogenic properties of various antimony compounds are limited (Filella et al., 2009); however, it is established that antimony is toxic (Gebel, 1997) and is a potential human carcinogen (Léonard and Gerber, 1996; Gebel, 1997; Beyersmann and Hartwig, 2008).

Antimony is used in a wide variety of materials and applications: according to the 2012 United States Geological Survey (USGS) Mineral Commodity Summaries, the utilization of antimony by the US in 2011 was approximately 26,600 metric tons (Carlin, 2012). Antimony is commonly used as a hardener in lead/antimony alloys for bullets. Within the US approximately 80,000 tons of lead per year went to the production of ammunition in the late 1990s (US EPA Report, 2005).

Based on chemical analysis, 0.22 caliber (5.56 mm) bullets are comprised of, on average, 0.7 wt.% antimony (Randich et al., 2002), while 0.357 caliber (9 mm) rounds are comprised of up to 1.8 wt.% (Keto, 1999). Average antimony content in bullets of up to 2–5 wt.% has also been reported (Johnson et al., 2005). Assuming that, on average, a lead bullet contains 1 wt.% of antimony, a rough estimate can be made that ~800 tons of antimony is deposited yearly at shooting ranges in the US. While this is a small fraction of the total annual usage of antimony in the US, this antimony (and lead) are highly localized within target range soils, resulting in highly elevated concentrations at military and recreational shooting ranges (Basunia and Landsberger, 2001; Johnson et al., 2005; Olivé, 2006; Scheinost et al., 2006; Ackermann et al., 2009). Previously reported antimony levels in shooting range soils have been found to range from 1 to 517 mg kg^{-1} (Basunia and Landsberger, 2001) and up to 13,800 mg kg^{-1} (Johnson et al., 2005). These values greatly exceed typical crustal soil background values of a few mg kg^{-1} or less (Filella et al., 2009). Antimony concentrations found in a shooting range runoff are elevated, and positively correlate to water flow and dissolved organic carbon (Strømseng et al., 2009; Heier et al., 2010).

Antimony exists in two oxidation states (+3 or +5) under typical surface water and soil redox conditions. The mobility of antimony is limited by secondary mineral precipitation (Diemar et al., 2009; Filella and Williams, 2012; Roper et al., 2012), and partitioning to metal (hydr)oxides of Al, Fe, and Mn (Thanabalasingam and Pickering, 1990; Rakshit et al., 2011; Xu et al., 2011), clay minerals (Xi et al., 2010, 2011; Ilgen and Trainor, 2012), and humic acids (Pilarski et al., 1995; Tighe et al., 2005). Aqueous concentrations of Sb(III) are typically limited by the Sb_2O_3 phases sénarmontite (to 1.2 μM) and valentinite (to 10 μM) (Zotov et al., 2003), and Sb(V) by roméite – $Ca_2Sb_2O_7$ (Roper et al., 2012). The reported aqueous concentration of Sb(V) from dissolution of roméite is 0.33 ± 0.1 μM (Diemar et al., 2009). Due to these solubility constraints, antimony is considered relatively immobile in soil environments (Filella et al., 2002; Knechtenhofer et al., 2003; Diemar et al., 2009; Reimann et al., 2010).

Homogeneous oxidation of Sb(III) to Sb(V) by dissolved O_2 depends on pH and aqueous composition, and does not proceed at a measurable rate at pH < 9.8 after 200 days (Leuz and Johnson, 2005). The rate of Sb(III) oxidation by dissolved O_2 is promoted by the addition of aqueous Fe(II) (Leuz et al., 2006a), and the addition of the dissolved metals copper (Cu), manganese (Mn), and lead (Pb) was shown to catalyze oxidation of Sb(III) by hydrogen peroxide (Elleouet et al., 2005). In heterogeneous systems, oxidation of Sb(III) to Sb(V) is promoted by natural and synthetic amorphous iron (hydr)oxides (Belzile et al., 2001), synthetic goethite (Leuz et al., 2006b), and partially reduced iron-rich nontronite clay (Ilgen et al., 2012). Further studies are needed to understand chemical controls on antimony oxidation rates, particularly in heterogeneous systems.

Antimony is found in mineral deposits typically in the sulfide form (stibnite, Sb_2S_3) or one of the associated oxidation products. The typical mineral sequence observed during oxidation and dissolution of stibnite is: stibnite → kermesite (Sb_2S_2O) → sénarmontite/valentinite → cervantite (Sb_2O_4) → roméite group minerals (Roper et al., 2012). In natural systems, the oxidation is relatively fast as indicated by the predominance of oxidized Sb(V) species downstream from stibnite bearing deposits (Ashley et al., 2003; Liu et al., 2010; Beauchemin et al., 2012; Ritchie et al., 2013), and the main pathway for antimony removal from the water column is sorption and co-precipitation with iron (hydr)oxides (Ashley et al., 2003; Beauchemin et al., 2012; Ritchie et al., 2013). There are fewer studies of antimony oxidation in shooting range soils compared to the number of studies of the fate and transport of antimony associated with sulfide deposits.

A unique aspect of trace metal deposition into shooting range soils is that they are "loaded" to the target berms through impact of a rapidly moving projectile. On impact the metallic bullets are shattered, exposing fresh surfaces that are expected to undergo fast oxidation under surface soil conditions. Based on the spectroscopic study by Scheinost et al. (2006) exclusively Sb(0) and Sb(V) adsorbed to iron (hydr)oxides was found in shooting range soils in Switzerland with no Sb(III)-containing solid phases observed (Scheinost et al., 2006; Ackermann et al., 2009). Similarly, exchangeable and specifically adsorbed fractions of antimony extracted from heavily polluted soils and river sediments (district of Příbram, Czech Republic) were found to be in the oxidized Sb(V) form, except for acidic soils with a high organic content, where the fraction of Sb(III) varied from 3% to 33% of the total antimony content (Ettler et al., 2007). In laboratory experiments, an electrode potential sweep from −0.2 to 10 V with Sb(0) at pH 7 (in phosphate buffer) resulted in formation of an oxide film, which is composed exclusively of Sb(III) as determined by ellipsometry and X-ray photoelectron spectroscopy (Linarez Pérez et al., 2010).

Uncertainty remains as to why Sb(III)-containing solid phases are not observed in soils with corroding Sb-containing bullets investigated up to date (Scheinost et al., 2006; Ackermann et al., 2009), while they are commonly observed as a result of stibnite oxidation, e.g. sénarmontite and valentinite (Roper et al., 2012), and during Sb(0) oxidation in laboratory studies (Linarez Pérez et al., 2010). To further improve the overall understanding of the factors controlling

the Sb(0) → Sb(III) → Sb(V) oxidation sequence in heterogeneous systems we designed and implemented a set of batch experiments to study the oxidation and dissolution of Sb(0) as a function of solution composition. We also tested how the addition of Pb(0) affects the oxidation and mobilization of antimony and characterized the oxidation products which may serve as a secondary source or control on aqueous concentrations of antimony. We chose to use simple solution chemistry with constituents commonly present in soil/groundwater systems. Iron was excluded from the experiments in order to focus on the primary oxidation products of the metallic phases. We also tested the role of a complexation on directing the reaction pathway of oxidation and solubility of antimony using a model organic ligand – disodium salt of ethylenediaminetetraacetic acid (EDTA). The results presented here provide information to help constrain our understanding of the reaction pathways during incipient oxidation of metallic antimony.

2. MATERIALS AND METHODS

2.1. Experimental procedures

All solutions were prepared using Milli-Q H_2O (resistivity of 18.2 MΩ cm, filtered to less than 0.2 μm and UV-irradiated; Barnstead NANOpure DIamond). We refer to the Milli-Q water as DI (deionized) water for brevity. Stock solutions included 100 mM disodium salt of ethylenediaminetetraacetic acid (disodium EDTA), 100 mM sodium nitrate, 100 mM calcium nitrate, 55 μM antimony trichloride [Sb(III)], and 5 mM potassium (pyro)antimonate [Sb(V)]. Stock solutions were prepared by dissolving $C_{10}H_{14}O_8N_2Na_2{\cdot}2H_2O$ (99.5%), $NaNO_3$ (ACS grade), $Ca(NO_3)_2$ (ACS grade), $SbCl_3$(99.4% ACS grade), and $KSb(OH)_6$ (98%) in DI H_2O, and then filtering the solutions through 0.45 μm Whatman Nylon membrane disposable filters. For the Sb(III) stock solution we used deoxygenated DI H_2O (boiled for 45 min and purged with N_2 gas during cooling). Antimony trichloride stock solution was stored at 4 °C in an amber glass bottle away from light prior to use.

The simulated groundwater (SGW) was prepared by dissolving $CaCO_3$ (99+%) and NaCl (reagent grade) in DI H_2O, then the pH was adjusted to 7.0 with ultrapure HNO_3. The SGW composition was verified by ion chromatography (IC) analysis to be 0.29 mM Na^+, 1.24 mM Ca^{2+}, 0.28 mM Cl^-, 1.97 mM NO_3^-, and 0.062 mM HCO_3^-.

Batch reactors with Sb(0) and Pb(0) were prepared in 50 mL polypropylene centrifuge tubes. The experiments were performed at 20 °C in equilibrium with the atmosphere, light was not excluded, and pH (not buffered) was measured using a Thermo ORION meter with a combination pH electrode (PerpHectRoss). The initial pH measurement was taken 5–30 min after all the components were combined in the reactors and then pH was measured every time a sample was collected. The Sb(0) and Pb(0) powders (200 mesh size) were allowed to react for a maximum of 222 days. The net composition of the batch reactors is shown in Table 1. Duplicate batches for the DI/Sb and SGW/Sb reactors were set up and sampled 3 times between 41 and 192 h of equilibration in order to determine the reproducibility of our results. An additional sample was made with Pb(0) powder (2.0 g), which was allowed to oxidize in 100 mL of DI H_2O by purging with air for 48 h in a glass beaker. The reactors were sampled at increasing time intervals to follow a logarithmic time sequence. During sampling a 2–3 mL volume was collected, each sample was filtered through a 0.45-μm Whatman Nylon membrane disposable filter, and samples were immediately analyzed by liquid chromatography inductively coupled plasma-mass spectrometry (LC-ICP-MS).

2.2. Aqueous sample analysis

The oxidation state of antimony in aqueous samples was determined using LC-ICP-MS. Speciation standards were made prior to each analytical run by diluting antimony stock solutions with DI H_2O so that the Sb(III) or Sb(V) concentration range was 0–1.24 μM (0–150 μg L^{-1}). The total concentration of antimony in these standards was verified by ICP-MS analysis prior to LC analysis. The resulting calibration curves included five standards for each Sb(III) and Sb(V) and had an R^2 value of 0.98 or higher. Calibration was performed prior to each analytical run of 20–50 samples. To determine the standard deviation of the measurement we analyzed one sample and one standard solution three times during each analytical run. The Sb(III) and Sb(V) were separated using an arsenic speciation column (Agilent G3154-65001, 150 mm × 4.6 mm i.d.) and guard column (Agilent G3154-65002, 4.6 mm × 10 mm i.d.) packed with chemical bonded hydrophilic anion exchange resin. The mobile phase consisted of 12 mM Na_2EDTA, 2 mM phthalic acid and 3 vol.% methanol, the resulting pH was ~4.5 [modified from Zheng et al. (2001)]. As an internal standard we added an indium (^{115}In) ICP-MS standard solution to the mobile phase at 0.43 μM (50 μg L^{-1}). The radio frequency (RF) power was set at 1500 W, and sample injection volume was 100 μL. The flow rate of the mobile phase through the column was 1 mL min^{-1}. The detector count time for ^{121}Sb and ^{123}Sb was 0.5 s per point; total acquisition time was 450 s. The Sb(III) and Sb(V) peaks eluted at 210 and 130 s, respectively.

Areas under antimony peaks were integrated and background was subtracted using the Microcal Origin 6.0 software package. Antimony (^{121}Sb) counts were normalized by the internal standard (^{115}In) counts. The detection limit was ~8 nM (1 μg L^{-1}) for both Sb(III) and Sb(V). The Sb(V) standards were pure with no detectable Sb(III). Freshly prepared Sb(III) standards typically had a minor Sb(V) impurity of 8–16 nM (1–2 μg L^{-1}). The Sb(III) calibration curve was corrected by subtracting the Sb(V) impurity from the Sb total value obtained by the ICP-MS analysis.

The simulated groundwater was analyzed by ion chromatography (IC) using a Dionex ICS-3000 with an AS-19 anion column and a CS-12 cation column (Dionex). The injection volume of each sample was 10 mL. For anion analyses concentration of the potassium hydroxide eluent was gradually increased from 20 to 35 mM. Cation analyses

Table 1
Experimental conditions for the antimony metal oxidation batch reactors. The experiments were performed at 20 °C in equilibrium with atmosphere and light was not excluded. The pH was measured during sampling.

Batch reactor	DI/Sb	SGW/Sb[a]	SGW/Sb/EDTA	DI/Sb/Pb	DI/Sb/Pb/EDTA	DI/Sb/$Ca(NO_3)_2$	DI/Sb/$NaNO_3$
Medium	DI H_2O	SGW	SGW	DI H_2O	DI H_2O	DI H_2O	DI H_2O
Sb(0), g	0.100	0.100	0.100	0.050	0.050	0.100	0.100
Pb(0), g	\	\	\	0.050	0.050	\	\
EDTA, mM	\	\	10	\	10	\	\
Na^+, mM	\	0.29	20.29	\	20.0	\	10
Ca^{2+}, mM	\	1.24	1.24	\	\	10	\
NO_3^-, mM	\	1.97	1.97	\	\	20	10
Cl^-, mM	\	0.28	0.28	\	\	\	\
Max rxn time, days	222	222	146	146	146	146	146
Ionic strength, M	10^{-7}	3.8×10^{-3}	1.38×10^{-2}	2.58×10^{-4}[b]	1.0×10^{-2}	3.0×10^{-2}	1.0×10^{-2}
γ $(z \pm 1)$[c]	1.00	0.94	0.89	0.98	0.90	0.85	0.90
γ $(z \pm 2)$[c]	1.00	0.88	0.79	0.96	0.81	0.72	0.81

[a] Simulated groundwater (SGW): $[Na^+] = 0.29$ mM, $[Ca^{2+}] = 1.24$ mM, $[Cl^-] = 0.28$ mM, $[NO_3^-] = 1.97$ mM; $[HCO_3^-] = 0.062$ mM.
[b] Estimated based on the Pb(II) aqueous concentration derived from the solubility of hydrocerussite $Pb_3(CO_3)_2(OH)_2$.
[c] Activity coefficient calculated using Davies equation $-\log\gamma = Az^2\left[\frac{I^{1/2}}{1+I^{1/2}} - 0.2I\right]$.

were performed in isocratic mode with a concentration of the methane sulfonic acid eluent of 25 mM. The system flow rate was 1 mL min^{-1} and the conductivity cell temperature was 30 °C. The ion chromatograph was calibrated through repeat analysis of calibration and laboratory analytical standards. Based on these analyses the calculated precision for the analyses is ±5%. Peaks were identified using Chromeleon (Dionex) and verified visually. The composition of the simulated groundwater is provided in Table 1.

2.3. Solid sample analysis

Extended X-ray absorption fine structure (EXAFS) data was collected at bending magnet beamline sector 13 BM (GSECARS), Advanced Photon Source (APS), Argonne National Laboratory. The Si(111) water-cooled monochromator was calibrated at the mid-point of the antimony K-edge (peak of derivative spectrum) at 30,491 eV using an Sb(0) reference foil. For harmonic rejection we used a platinum mirror and detuned the monochromator by 20%. The monochromator step size was 5 eV in the pre-edge, 0.5 eV in the near edge region, and 0.05 $Å^{-1}$ in the EXAFS region. The counting time was 2 s per point with increasing counting time at higher k-values (a power of 3 was applied). The spectra for all samples were recorded in transmission mode using ionization chambers (I_0 and I_1) with an Sb(0) reference foil placed in line downstream of the sample (I_2). These reference spectra were used to correct for possible monochromator drift. The ionization chambers I_0, I_1, and I_2 were filled with argon gas. The samples were scanned 2–4 times and the data was averaged.

The EXAFS data was processed and modeled using the Athena and Artemis interface (Ravel and Newville, 2005) to the IFEFFIT (Newville, 2001) program. The background subtraction (AUTOBK algorithm; Newville et al., 1993), normalization and conversion into k-space were conducted as described elsewhere (Kelly et al., 2008). The Fourier transform (Hanning window, *dk* value of 1) was applied to Sb K-edge EXAFS data over the k-range of approximately 2.5–12.5. The Fourier transformed antimony K-edge EXAFS spectra were analyzed using Artemis by fitting theoretical paths calculated with Feff 6 (Zabinsky et al., 1995; Newville, 2001) based on the structure of sénarmontite (Whitten et al., 2004) and Sb(0) (Wyckoff, 1963). The amplitude reduction factor (S_0) was fixed at 0.97, based on fitting $KSb(OH)_6$ model compound EXAFS spectra recorded during the same analytical run.

To identify crystalline phases forming as a result of Sb(0) and Pb(0) oxidation in the batch reactors, randomly orientated dried sample powders were analyzed by X-ray powder diffraction (XRD). We used an X'Pert PRO Material Research Diffractometer (PANalytical) equipped with either a Cu (Kα $\lambda = 1.54277$ Å), or Co (Kα $\lambda = 1.79082$ Å) X-ray tube with the generator set at 45 kV and 40 mA, or 40 kV and 45 mV, respectively. Scans were collected from 5 to 100° 2θ and a counting time of 60 s per point at either 0.002 or 0.013° step size. Diffraction patterns collected with Cu radiation were an average of five repeated scans. All diffraction patterns were processed using PANalytical's X'Pert HighScore Plus 2.2 software package and Bragg peaks were matched using the PDF-4+ 2012 database (ICDD). In addition, the fraction of crystalline phases in the diffraction patterns of partially reacted DI/Sb and SGW/Sb batch reactors (analyzed with Cu radiation) were determined semi-quantitatively using the normalized Reference Intensity Ratios method (Chung, 1974a,b, 1975; Snyder, 1992).

The oxidized antimony powders from the reactors DI/Sb and SGW/Sb were dried in the air and imaged using an ISI-SR-50 Scanning Electron Microscope (SEM) at 20 keV and original magnification of 1000×. No coating or other sample treatments were used. The surface areas of Sb(0) (99.999%) and Pb(0) (99.9%) metal powders were determined using the Brunauer–Emmett–Teller (BET) N_2 adsorption method. The Sb(0) (0.366 g) and Pb(0) (0.244 g) powders were out-gassed under vacuum at

300 °C for 60 min prior to the analysis. The specific surface area measured by BET was 0.59 $m^2 g^{-1}$ for Sb(0) and 2.67 $m^2 g^{-1}$ for Pb(0) powders.

2.4. Thermodynamic modeling

The software package Geochemist Workbench (GWB) (Bethke, 1998) was used for thermodynamic modeling. To account for all relevant antimony and lead aqueous and mineral species we modified the Lawrence Livermore National Lab (LLNL) V8 R6 thermodynamic dataset. We included the $Sb(OH)_6^-$ aqueous species with the equilibrium constant for Sb(III)/Sb(V) couple calculated based on the tabulated standard redox potential (Lide, 1993), H_4-EDTA dissociation constants (Lide, 1993), PbH_2EDTA complexation constant (Martell and Smith, 1974), $CaHEDTA^-$ complexation constant (Martell and Smith, 1974), and SbHEDTA complexation constant (Filella and May, 2005). We also added the mineral phases mopungite ($NaSb(OH)_6$) (Blandamer et al., 1974), sénarmontite (Sb_2O_3) and valentinite (Sb_2O_3) (Zotov et al., 2003).

The experimental data collected on all batch reactors was used to model the path of reaction during the oxidation of Sb(0). We used the React module of the GWB for these calculations. The composition of the batch reactors (Table 1) and initial pH were used as input, and Sb(0) and Pb(0) were added as reactant species. Temperature was fixed at 25 °C and partial pressure of $CO_2(g)$ was fixed at 0.38×10^{-3} atm. Since measured concentrations of Sb(III) and Sb(V) aqueous species indicate that systems were at thermodynamic disequilibrium, we de-coupled Sb(III)/Sb(V), and set the Eh value at the completion of the reaction at 0.45 V.

3. RESULTS AND DISCUSSION

3.1. Speciation of antimony and lead in the solid phase oxidation products

The XRD patterns of the fresh and partially oxidized (1 and 5 months reaction time) antimony metal powders are shown in Fig. 1. The XRD patterns for the solid phases collected from all batch reactors at the completion of the experiment are shown in Figs. 1 and 2. The semi-quantitative analysis of the XRD data indicated that the extent of Sb(0) oxidation is more pronounced in the reactor with simulated groundwater (SGW/Sb) compared to the reactor with DI water (DI/Sb). Sénarmontite was the predominant crystalline oxidation product identified in all reactors with the exception of the DI/Sb/Pb reactor where the extent of Sb(0) oxidation was least pronounced and no crystalline phases, besides the starting materials, were found. In addition, the Sb(V) phase mopungite was identified in the reactor SGW/Sb/EDTA. Some antimony metal remained in all

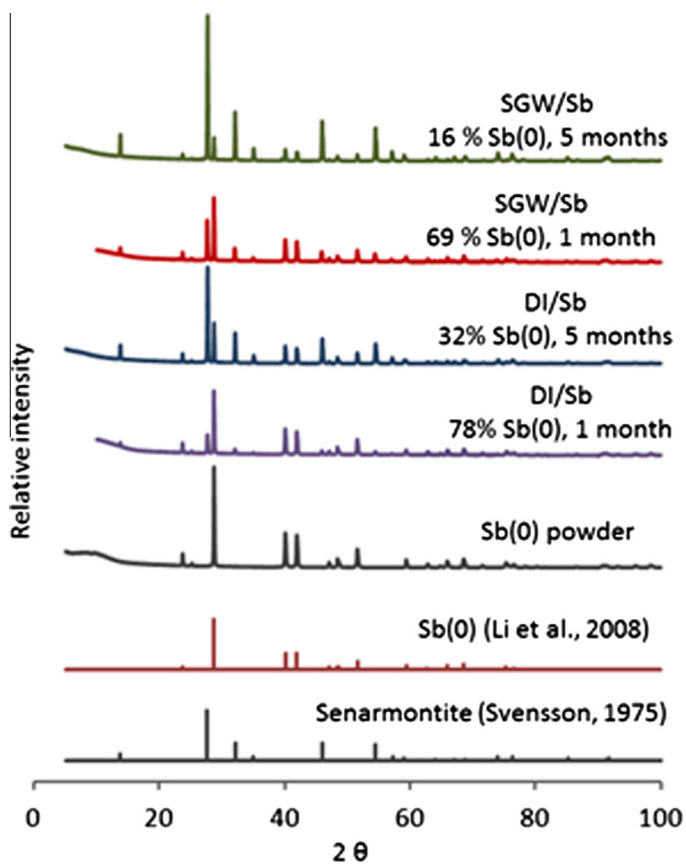

Fig. 1. X-ray diffraction (Cu Kα) patterns collected on solid phases from the DI/Sb and SGW/Sb reactors after 1 month and 5 months from the beginning of experiment. Percentage of remaining Sb(0) is calculated semi-quantitatively using the normalized Reference intensity ratios method (Chung, 1974a,b, 1975; Snyder, 1992). Patterns for the reference phases (Sb metal and sénarmontite) are also shown.

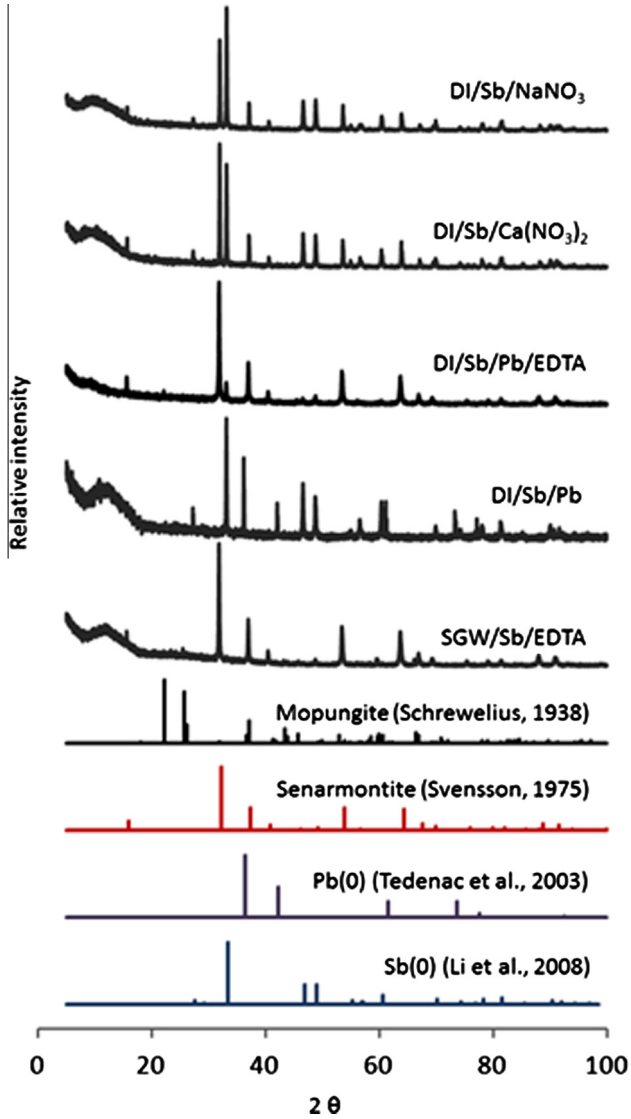

Fig. 2. X-ray diffraction (Cu Kα) patterns collected on solid phases from the remaining batch reactors by the completion of experiment after 5 months. Patterns for the reference phases (Sb and Pb metals, sénarmontite and mopungite) are also shown.

Table 2
Mineral phases identified by X-ray diffraction (XRD) in the Sb(0) batch reactor experiments.

Batch reactors							
Mineral phase	DI/Sb	SGW/Sb	SGW/Sb/EDTA	DI/Sb/Pb	DI/Sb/Pb/EDTA[a]	DI/Sb/Ca(NO_3)$_2$	DI/Sb/$NaNO_3$
Sb(0)	+	+	+	+	+	+	+
Senarmontite	+	+	+		+	+	+
Mopungite			+				
Pb(0)				+			

[a] Evidence for presence of hydrocerussite and litharge is inconclusive due to weak diffraction pattern and overlap of Bragg peaks with more abundant phases.

reactors after five months. The list of crystalline phases found in each batch reactor is shown in Table 2. The oxidized lead metal powder (oxidized in 100 mL of DI H_2O by purging with air for 48 h) was analyzed by XRD, and hydrocerussite was the predominant crystalline phase (data not shown).

The EXAFS data for Sb(0), sénarmontite, and the post-reaction solids collected after five months of reaction from the DI/Sb and SGW/Sb batch reactors and corresponding fits are shown in Fig. 3. The EXAFS fitting parameters are summarized in Table 3. In agreement with the XRD findings, shell-by-shell fitting of the backscattering features

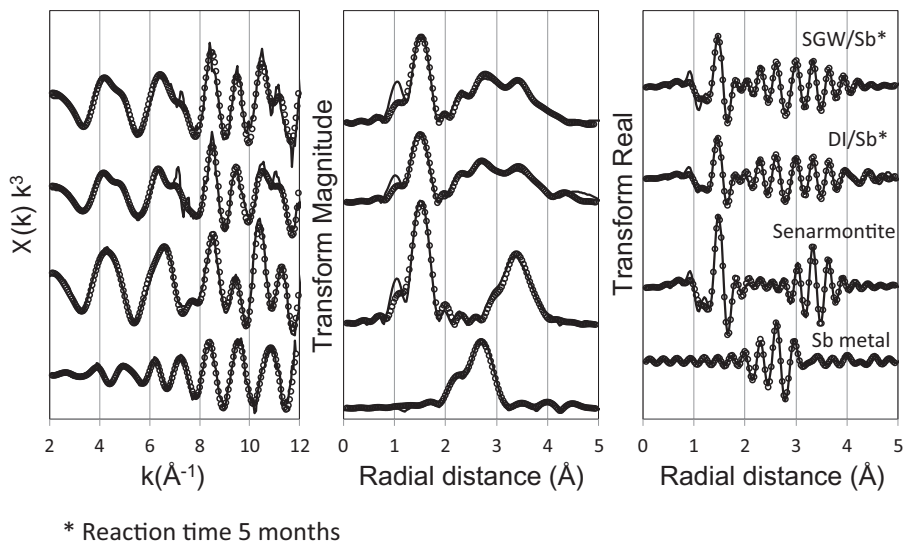

Fig. 3. Extended X-ray absorption fine structure spectra (solid lines) and fit (empty circles) for antimony metal, sénarmontite, and the post-reaction solids collected after 5 months of reaction from the DI/Sb and SGW/Sb batch reactors.

Table 3
Fitting parameters for the extended X-ray absorption fine structure (EXAFS) spectra. Fitting was done in *R*-space; *k*-weights of 1, 2, and 3 were fitted simultaneously, the amplitude reduction factor (S_0) was set at 0.97. Error at a 95% confidence level is shown in parenthesis.

Sample	*k*-range[a]	*R*-range (Å)	Shell	CN[b]	*R* (Å)[c]	σ^2 (Å^2)[d]	ΔE_0 (eV)[e]	*R*-factor[f]	Red χ^2 [g]	Ind. Pts.[h]
Senarmontite	2.7–12.6	1.0–4.5	Sb–O	3.6(2)	1.97(1)	0.003(1)	8.3(7)	0.006	243	22
			Sb–Sb	2.4(5)	3.61(1)	0.003(1)				
			Sb–Sb	1.1(7)	3.96(3)	0.004(3)				
Antimony metal	1.8–11.7	1.0–5.0	Sb–Sb	1.8(2)	2.89(1)	0.003(1)	6(1)	0.046	48.6	25
			Sb–Sb	0.8(3)	3.32(2)	0.003(2)				
			Sb–Sb	1.6(6)	4.31(2)	0.003(2)				
			Sb–Sb	1.7(7)	4.48(2)	0.003(2)				
SGW/Sb (5 months)	2.8–12.0	1.0–5.0	Sb–O	1.8(1)	1.97(1)	0.003(1)	10.3(7)	0.009	27	23
			Sb–Sb	1.0(1)	2.91(1)	0.003(1)				
			Sb–Sb	0.7(3)	3.35(2)	0.004(2)				
			Sb–Sb	1.4(3)	3.61(1)	0.004(1)				
			Sb–Sb	0.5(5)	3.93(6)	0.005(6)				
			Sb–Sb	0.5(6)	4.24(8)	0.005(7)				
DI/Sb (5 months)	2.7–11.9	1.0–4.5	Sb–O	1.4(1)	1.96(1)	0.004(1)	9(1)	0.008	57	20
			Sb–Sb	0.7(1)	2.89(1)	0.002(1)				
			Sb–Sb	0.8(2)	3.36(1)	0.004(1)				
			Sb–Sb	1.5(3)	3.60(1)	0.004(1)				
			Sb–Sb	0.8(4)	3.90(2)	0.004(2)				
			Sb–Sb	1.3(6)	4.36(2)	0.006(2)				

[a] Usable *k*-range.
[b] Coordination number.
[c] Bond length.
[d] Debye–Waller factors: mean-square amplitude reduction factor, including thermal and static disorder components.
[e] Energy shift between the theoretical and measured spectrum.
[f] *R*-factor (mean square misfit) $R_{\text{factor}} = \frac{\sum_i (\text{data}_i - \text{fit}_i)^2}{\sum_i \text{data}_i^2}$.
[g] Reduced chi-square $\chi_\upsilon^2 = \frac{N_{idp}}{N_{pts}} \sum_i \left(\frac{\text{data}_i - \text{fit}_i}{\varepsilon_i}\right)^2 / (N_{idp} - N_{var})$.
[h] Independent points (number of data points minus number of variable parameters) $N_{idp} = N_{pts} - N_{var}$.

was consistent with the structures of sénarmontite (Sb–O at 1.97(1) Å, Sb–Sb at 3.61(1) Å, and 3.96(3) Å), and metallic antimony (Sb–Sb at 2.89(1) Å, 3.32(2) Å, 4.31(2) Å, and 4.48(2) Å). If a minor amount of mopungite (found in the SGW/Sb/EDTA reactor by XRD, but not in the SGW/Sb reactor) was present, we would likely not be able to identify it due to lack of pronounced backscattering features in the fine structure of this mineral (Scheinost et al., 2006).

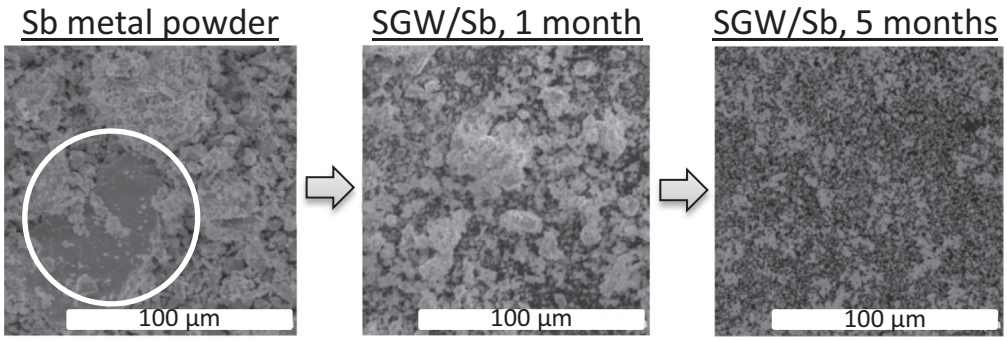

Fig. 4. Scanning electron microscopy images of the reacted Sb(0) powders (SGW/Sb) illustrate decrease of the particle size with increasing reaction time. Images were taken at 20 keV and original magnification of 1000×.

The particle size of the oxidized Sb(0) solid phases decreased with time based on the SEM images taken at different stages of the experiment (time = 0, 1 and 5 months) from the reactors DI/Sb and SGW/Sb (Fig. 4). This qualitative evidence supports significant oxidation of antimony metal powder, dissolution, and secondary mineral precipitation. Initially, Sb(0) powders had a variety of grain sizes, and larger particles with flat surfaces were present. After one month of reaction the grain size decreased and fewer flat surfaces were found. After 5 months of reaction the grain size decreased further compared to the 0 and 1 month samples.

3.2. Dissolution and aqueous speciation of antimony as a function of time

Metallic antimony readily generated dissolved Sb(III) and Sb(V) through oxidation and dissolution (Fig. 5). After 5–15 min of reaction the aqueous concentration of antimony in seven batch reactors reached 50–600 µM, with Sb(III) making up 96–100% of the total dissolved antimony. The total dissolved antimony measured in the duplicate reactors DI/Sb-duplicate, and SGW/Sb-duplicate (data not shown) was within the calculated analytical error of the concentrations in the DI/Sb and SGW/Sb reactors, respectively. The changes in the aqueous Sb(III) concentration with time in the batch reactors are shown in Fig. 6. The Sb(III) concentration profiles for the DI/Sb, SGW/Sb, DI/Sb/Pb, DI/Sb/$Ca(NO_3)_2$, and DI/Sb/$NaNO_3$ batch reactors show similar time dependence with an initial rapid increase (at 5–24 h) in the aqueous Sb(III) followed by a decrease for the remaining time of the experiment. The addition of an organic ligand, disodium EDTA, hindered the oxidation of Sb(III) to Sb(V) in the SGW/Sb/EDTA and DI/Sb/Pb/EDTA reactors, and, therefore, the concentration of Sb(III) kept increasing with time (Fig. 6).

The amount of total dissolved antimony and the extent of Sb(III) oxidation to Sb(V) depends on the composition of the aqueous matrix and on the addition of Pb(0) powder. The extent of Sb(III) oxidation to Sb(V) was larger in the system with simulated groundwater (SGW/Sb) compared to DI water (DI/Sb) and the extent of oxidation further decreased with added Pb(0) (DI/Sb/Pb). The low Sb(V) concentration in the DI/Sb/Pb batch reactor and absence of Sb(III) and Sb(V) solid phases based on the XRD analysis indicate that addition of Pb(0) inhibits the oxidation of Sb(0). Two plausible explanations for this observation include: (1) Pb(0) buffered the redox potential of the system, making it too reducing for Sb(0) to oxidize, and (2) Pb(0) oxidation products were deposited on the Sb(0) particles

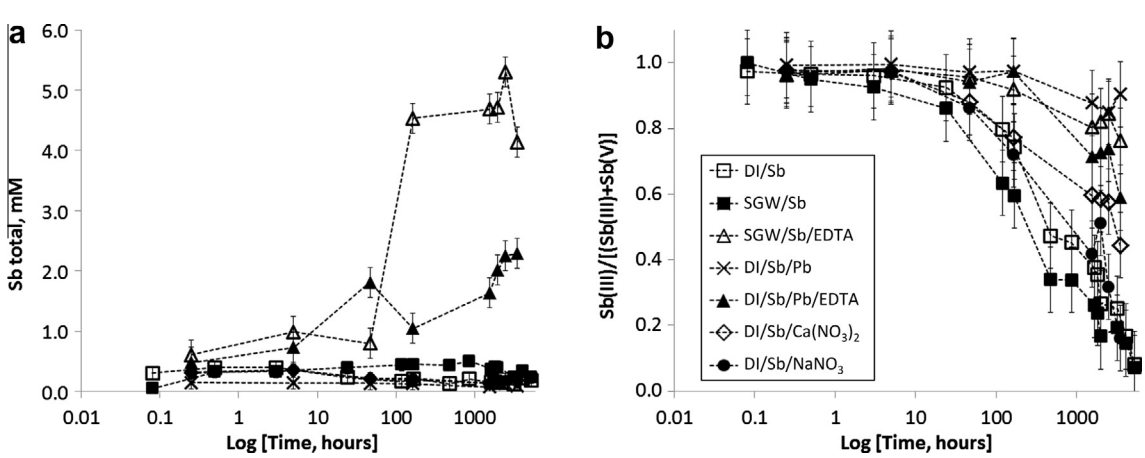

Fig. 5. Antimony oxidation and dissolution in batch reactors as a function of time: (a) Changes in the concentration of total dissolved antimony; (b) Changes in the fraction of Sb(III) in total dissolved antimony.

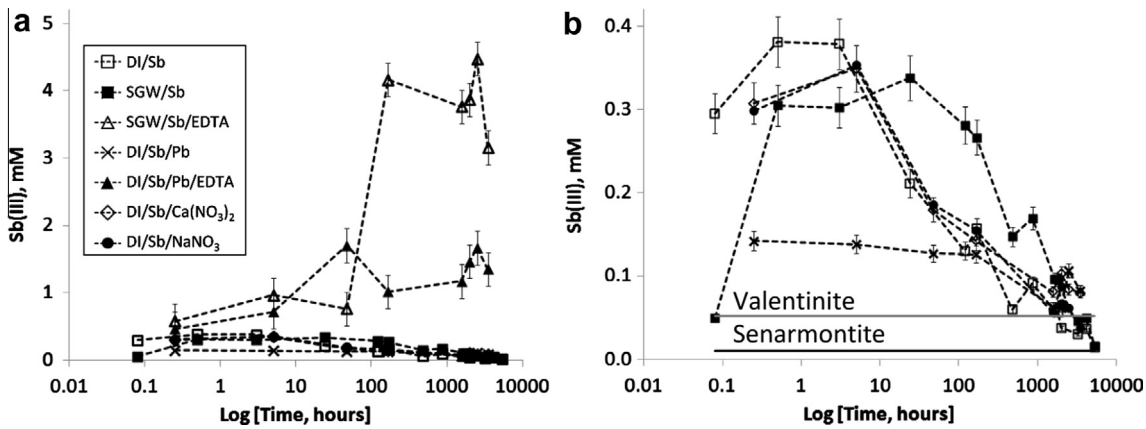

Fig. 6. Changes in aqueous Sb(III) concentration with time in the batch reactors: (a) All reactors, and (b) A subset of the reactors with solid lines indicating concentration of $Sb(OH)_3^0$(aq) in equilibrium with Sb_2O_3 polymorphs sénarmontite and valentinite.

Table 4
Solubility of Sb(III) and Sb(V) phases considered in this study (temperature 298.15 K, pressure 101.325 kPa).

Solid phase	Ksp	log Ksp	Sb (mol dm^{-3})	Reference
Senarmontite Sb_2O_3	$[Sb(OH)_3]$	−4.98		Zotov et al., 2003
Valentinite Sb_2O_3	$[Sb(OH)_3]$	−4.28		Zotov et al., 2003
Mopungite $NaSb(OH)_6$	$[Na^+] \times [Sb(OH)_6^-]$	−4.996		Blandamer et al., 1974
Romeite $Ca_2Sb_2O_7$	N/A[a]	N/A[a]	$3.3 \pm 1.0 \times 10^{-7}$	Diemar et al., 2009
Bindheimite $Pb_2Sb_2O_7$	N/A[a]	N/A[a]	$7.7 \pm 2.1 \times 10^{-8}$	Diemar et al., 2009
Hydrocerussite $Pb_3(CO_3)_2(OH)_2$	$[Pb^{2+}]^3 \times [CO_3^{2-}]^2/[H^+]^2$	−18.76		Visual MINTEQ thermo.vdb

[a] Incongruent dissolution was reported: Ca(II) and Pb(II) are dissolved preferentially by ion exchange, while Sb is poorly soluble (Diemar et al., 2009).

effectively passivating the Sb(0) particle surfaces. The first scenario is supported by the tabulated standard redox potentials involving Pb(0) and Sb(0):

$$Sb_2O_3 + 6H^+ + 6e^- \leftrightarrow 2Sb^0 + 3H_2O \quad E^0 = 0.152V(\text{Lide},1993) \tag{1}$$

$$PbO + H_2O + 2e^- \leftrightarrow Pb^0 + 2OH^- \quad E^0 = -0.580V(\text{Lide},1993) \tag{2}$$

where we expect Pb(0) oxidation to poise the system at a much more reducing condition than that favorable for Sb(0) oxidation.

The highest concentration of dissolved antimony was measured in the systems with added disodium EDTA (reactors SGW/Sb/EDTA and DI/Sb/Pb/EDTA) due to favorable Sb(III) complexation with EDTA. The SbHEDTA is the predominant Sb(III)–EDTA complex with a stability constant (β) of 10^{28} (Filella and May, 2005). The maximum measured Sb(III) was 4.48 mM, the concentration of added disodium EDTA was 10 mM, and the pH measured at the completion of the experiment was 5.62. Based on the

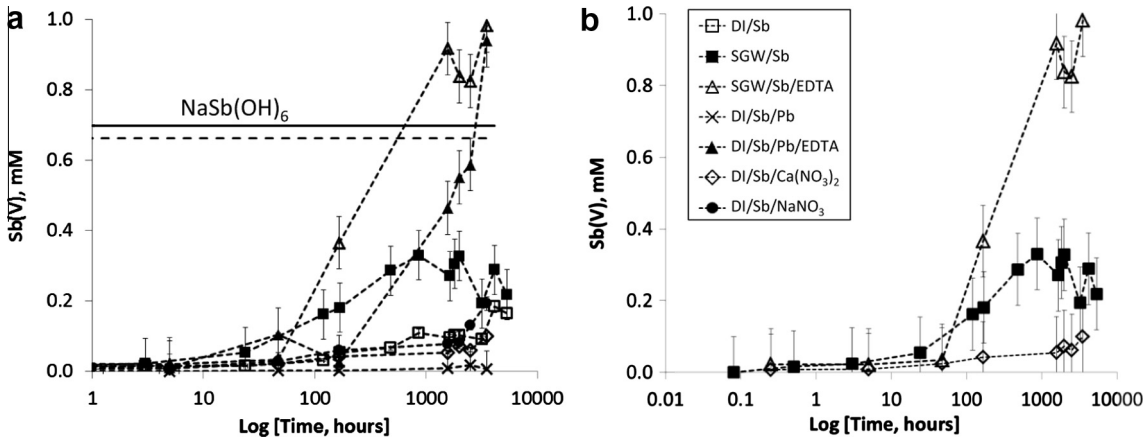

Fig. 7. Changes in aqueous Sb(V) concentration with time: (a) All reactors are shown, lines show calculated concentration of $Sb(OH)^{6-}$ in equilibrium with mopungite $NaSb(OH)_6$ in reactors SGW/Sb/EDTA – solid line at 6.98×10^{-4} M, and DI/Sb/Pb/EDTA – dashed line at 6.63×10^{-4} M; (b) Only reactors containing Ca^{2+} are shown.

stability constant, nearly all Sb(III) in the system was complexed with EDTA. In the system where both Pb(0) and EDTA were added the amount of aqueous Sb(III) was lower compared to the system without lead most likely due to Pb–EDTA complexation: the PbH_2EDTA complex stability constant (α) is $10^{17.88}$(Martell and Smith, 1974).

3.3. Solubility controls

The measured aqueous Sb(III) concentrations from five minutes up to approximately sixty-five days of reaction in all reactors show significant over-saturation with respect to the Sb_2O_3 polymorphs sénarmontite and valentinite. Based on the solubility data from Zotov et al. (2003), the equilibrium aqueous $Sb(OH)_3$ concentrations for sénarmontite and valentinite are 1.2 and 10 μM, respectively. By the completion of our experiment (146 or 222 days) the Sb(III) concentration decreased and solutions were slightly over-saturated with respect to sénarmontite, except for the reactors SGW/Sb/EDTA and DI/Sb/Pb/EDTA, where favorable complexation with EDTA resulted in the higher solubility of Sb(III) (Fig. 6). In Table 4 we summarize the solubility of the relevant Sb(III) and Sb(V) solid phases likely to form in our experiments based on the chemical constraints and the earlier observations of the secondary antimony minerals forming under low temperature, oxidizing conditions (Roper et al., 2012).

The changes in the aqueous Sb(V) concentration with reaction time are shown in Fig. 7. The predicted equilibrium concentration of $Sb(OH)_6^-$ is calculated based on the reported solubility of Sb(V) phases (Table 4) by taking into account the relevant activity coefficients (listed in Table 1). Since the concentration of Na^+ in four reactors vary from 0.29 to 20.29 mM (Table 1, reactors SGW/Sb, SGW/Sb/EDTA, DI/Sb/Pb/EDTA, and DI/Sb/$NaNO_3$), the calculated equilibrium Sb(V) concentrations with respect to

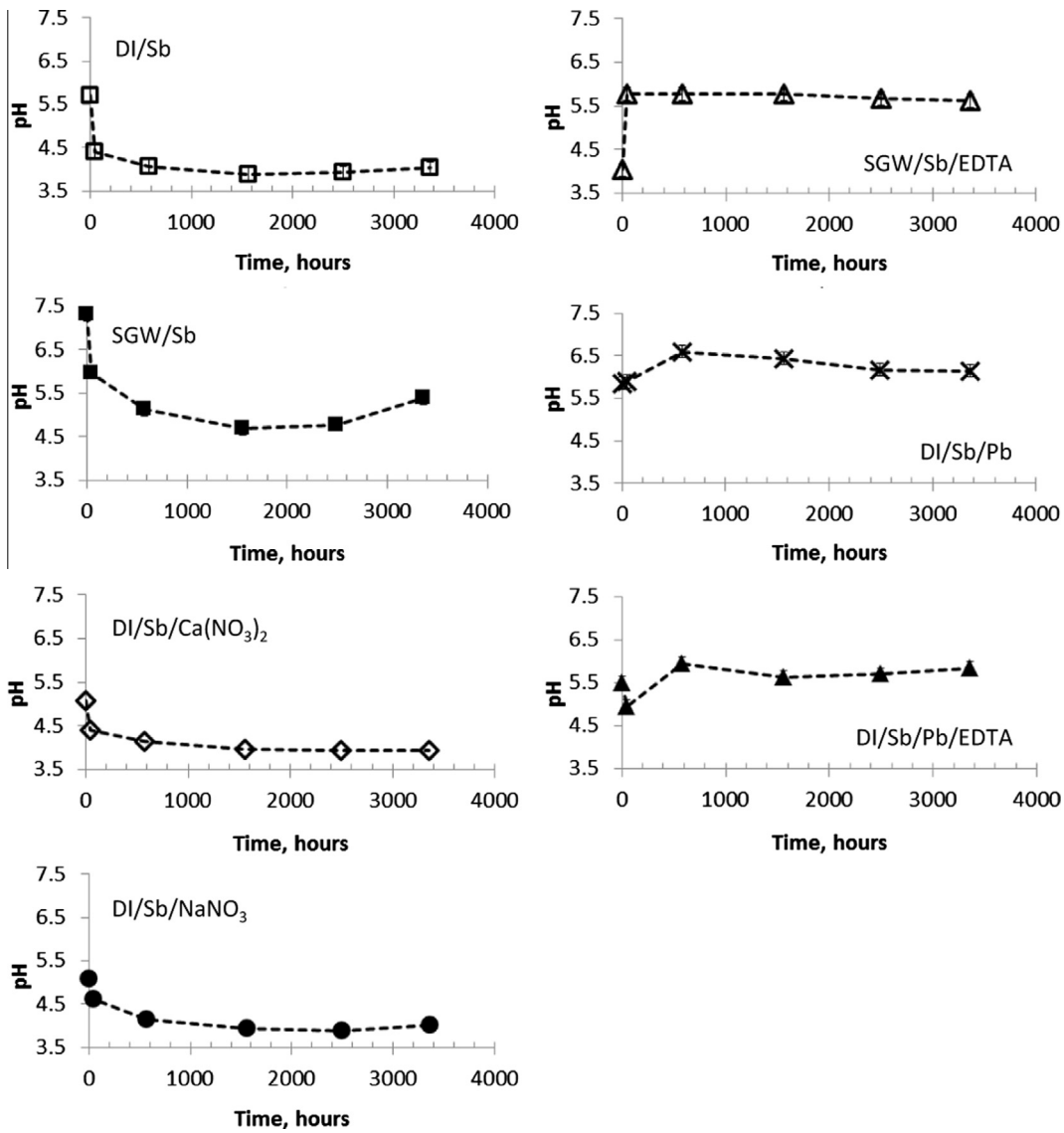

Fig. 8. Observed changes in pH over the course of the Sb(0) and Pb(0) oxidation experiments in the reactors with deionized (DI) water and simulated groundwater (SGW). The compositions of the batch reactors are given in Table 1.

mopungite are also different: 6.98×10^{-4} M (SGW/Sb/EDTA), 6.63×10^{-4} M (DI/Sb/Pb/EDTA), 1.25×10^{-3} M (DI/Sb/$NaNO_3$), and 3.94×10^{-2} M mM (SGW/Sb). At the completion of our experiment the measured Sb(V) concentration in the SGW/Sb/EDTA and DI/Sb/Pb/EDTA batch reactors was above the saturation limit with respect to mopungite. Mopungite was found in the SGW/Sb/EDTA reactor by XRD analysis but it was not found in the DI/Sb/Pb/EDTA reactor. The calculated equilibrium $Sb(OH)_6^-$ concentrations in the DI/Sb/$NaNO_3$

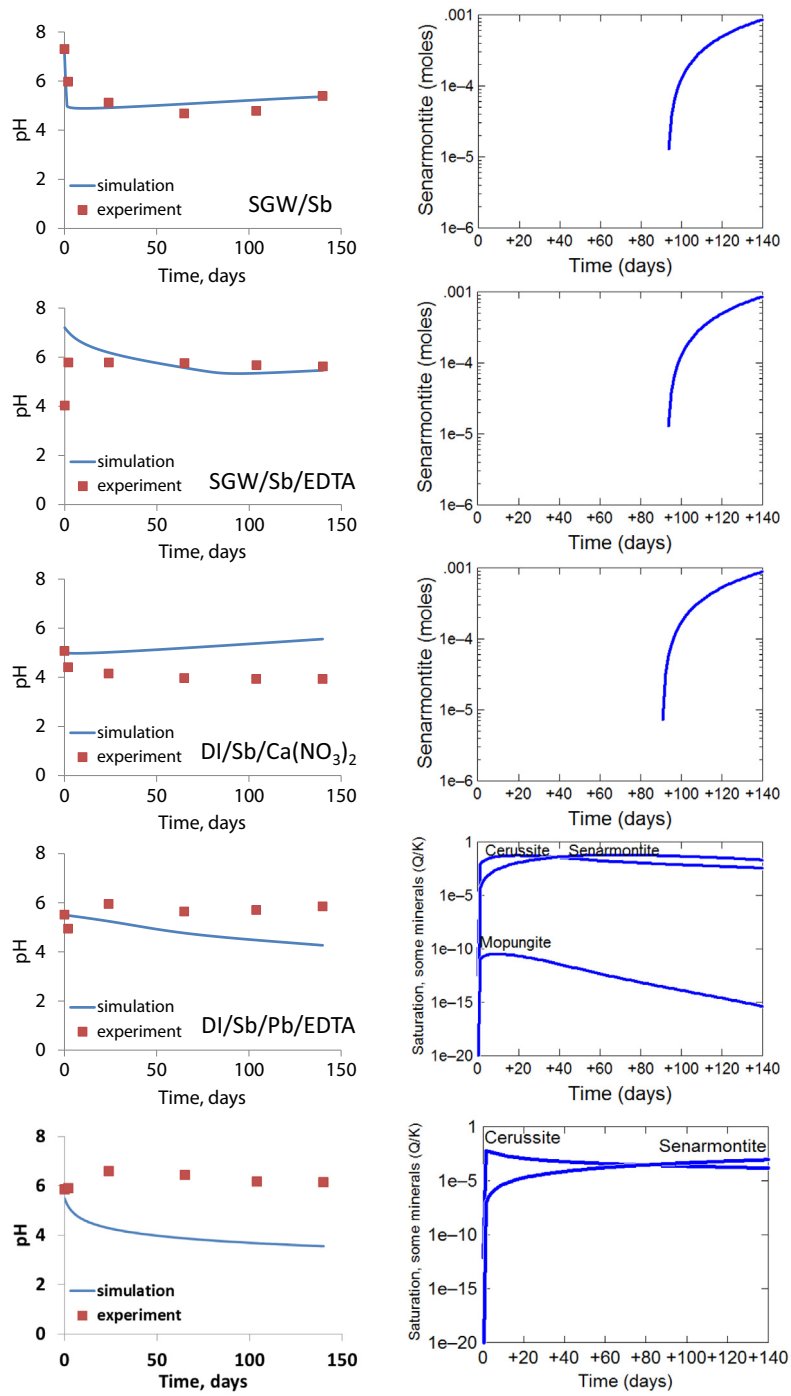

Fig. 9. Reaction path modeling results: graphs in the left column illustrate calculated (lines) and observed (points) pH; Graphs in the right column show mineral phases predicted to precipitate. Only sénarmontite is predicted to precipitate in the reactors DI/Sb (data not shown), DI/Sb/$NaNO_3$ (data not shown), SGW/Sb, SGW/Sb/EDTA, and DI/Sb/$Ca(NO_3)_2$. No secondary mineral precipitation is predicted for the DI/Sb/Pb/EDTA and DI/Sb/Pb batch reactors, therefore graphs for these reactors show calculated saturation index with respect to selected mineral phases.

(1.25×10^{-3} M) and SGW/Sb (3.94×10^{-2} M mM) reactors are higher than the measured Sb(V) (0.2–0.3 $\times 10^{-3}$ M), and, therefore, in agreement with the absence of mopungite in these samples.

The measured Sb(V) concentrations in the systems with Ca^{2+} (SGW/Sb, SGW/Sb/EDTA, and DI/Sb/$Ca(NO_3)_2$) were 0.33×10^{-3} mol L^{-1}, 0.98×10^{-3} mol L^{-1}, and 0.10×10^{-3} mol L^{-1} respectively, which is several orders of magnitude higher than measured in the roméite ($Ca_2Sb_2O_7$) dissolution experiments – $3.3 \pm 1.0 \times 10^{-7}$ mol dm^{-3} (Diemar et al., 2009). In the systems with Pb^{2+} (DI/Sb/Pb, and DI/Sb/Pb/EDTA) the measured Sb(V) concentration 0.87–1.88 $\times 10^{-5}$ M was about 3 orders of magnitude higher than the Sb(V) concentration of $7.7 \pm 2.1 \times 10^{-8}$ M measured during dissolution of bindheimite – $Pb_2Sb_2O_7$ (Diemar et al., 2009). Therefore, similarly to the Sb(III), precipitation of the Sb(V) solid phases was kinetically hindered.

3.4. Summary of the processes occurring in the batch reactors

The observed changes in pH with time are shown in Fig. 8. The pH shifts from near neutral (pH 6–7) to more acidic (pH 4–5) in the reactors DI/Sb, SGW/Sb, DI/Sb/$Ca(NO_3)_2$ and DI/Sb/$NaNO_3$ in the beginning (0–500 h) of our experiment. The pH increases in the reactors SGW/Sb/EDTA, DI/Sb/Pb, and DI/Sb/Pb/EDTA over the same time period (0–500 h). Based on the observations discussed in the previous sections, we propose that the following reaction scheme can be used to describe speciation and pH shifts observed in the batch reactors:

$$4Sb^0(s) + 3O_2(aq) + 6H_2O \rightarrow 4Sb(OH)_3(aq) \quad (3)$$

$$Sb(OH)_3(aq) + 0.5O_2(aq) + 2H_2O \rightarrow Sb(OH)_6^- + H^+ \quad (4)$$

$$Sb(OH)_3(aq) + 2H^+ + H_2EDTA^{2-} \rightarrow SbHEDTA(aq) + 3H_2O \quad (5)$$

$$Pb^0(s) + 0.5O_2(aq) + 2H^+ \rightarrow Pb^{2+} + H_2O \quad (6)$$

To further investigate this reaction scheme we used a reaction path model in GWB to simulate pH changes and phase precipitation as a function of reaction progress. The reaction path was simulated by titrating Sb(0) from zero to 5.0×10^{-3} moles in the reactors without Pb(0). The value of 5.0×10^{-3} moles was selected since Sb(0) did not fully react (based on the XRD data collected on the post-reaction solids), and this amount was estimated using the measurement of the highest aqueous concentration of antimony. In the simulation for the DI/Sb/Pb/EDTA reactor we set the amounts of Sb(0) and Pb(0) to 2.5×10^{-3} -moles each. Based on the overall lower Sb(total) concentration found in DI/Sb/Pb reactor, the amount of reacting Sb(0) was set at 0.1×10^{-3} moles, and Pb(0) at 2.5×10^{-3} moles. Based on the XRD analysis, no Sb_2O_4 and Sb_2O_5 phases were found in the oxidized Sb(0) samples. We suppressed the Sb_2O_4 and Sb_2O_5 phases during the reaction path modeling, as well as Sb_4O_6 (cubic) and Sb_4O_6 (orthorhombic) included in the LLBL thermodynamic database. The predicted pH change over the course of oxidation, and expected products for five batch reactors are shown in Fig. 9. Two reactors – DI/Sb and DI/Sb/$NaNO_3$ – are not shown since the modeling results for these reactors are nearly identical to the DI/Sb/$Ca(NO_3)_2$ reactor. The predicted and observed changes in pH agree extremely well (±0.5 pH units) for the SGW/Sb and SGW/Sb/EDTA reactors. For the remaining reactors the difference between predicted equilibrium pH and measured pH is 1.6–1.9 pH units at the completion of the run. This difference in pH is likely due to kinetic controls on the Sb(III) to Sb(V) oxidation – reaction (4). The predicted and experimentally observed mineral phases are also in general agreement. Precipitation of sénarmontite is predicted and observed in the reactors DI/Sb, SGW/Sb, SGW/Sb/EDTA, DI/Sb/$Ca(NO_3)_2$, and DI/Sb/$NaNO_3$. No minerals are expected to precipitate in the DI/Sb/Pb reactor, which agrees with the observation that no secondary mineral phases were detected by XRD. The only exception is the reactor DI/Sb/Pb/EDTA, where thermodynamic modeling results in no predicted mineral precipitation; however sénarmontite was observed using XRD. Calculated pH value in this reactor is 4.2, while measured pH was 5.6. If the model is run with pH fixed at 5.6, then cerrusite (not -observed) and sénarmontite (observed) are predicted to precipitate.

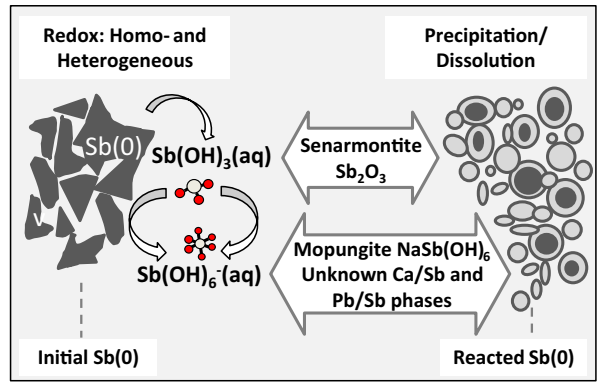

Fig. 10. Processes observed in the batch reactors: heterogeneous oxidation of Sb(0) to Sb(III) and, further, to Sb(V), homogeneous oxidation of Sb(III) to Sb(V), and precipitation/dissolution of the Sb(III) and Sb(V) phases.

The summary of the processes observed in this study is shown in Fig. 10. Several processes control the aqueous speciation and concentration of antimony: heterogeneous oxidation of Sb(0) to Sb(III) and, further, to Sb(V), homogeneous oxidation of Sb(III) to Sb(V), and precipitation/dissolution of the Sb(III) and Sb(V) phases. The rate of heterogeneous redox reactions depends on the surface area, while surface area is changing during the experiment due to dissolution of the initial material and secondary mineral precipitation.

4. CONCLUSIONS

The goal of this research was to examine some of the chemical processes that control the oxidation of metallic antimony under laboratory conditions. The obtained results contribute to the understanding of antimony fate and transport during the weathering of metallic lead/antimony bullets. Three main conclusions can be drawn from our work. First, the observed oxidation and dissolution of

antimony is rapid: after 5–15 min of reaction, the aqueous concentration reached 50–600 μM, with Sb(III) at 96.3–100% of the total dissolved antimony. Sénarmontite (Sb_2O_3) was the primary crystalline oxidation product, and it formed in all examined systems (with exception of DI/Sb/Pb reactor) as soon as one month from the beginning of the oxidation experiment. At the termination of the batch experiments after 146 or 222 days of reaction, the aqueous concentration of Sb(III) was controlled by sénarmontite. On a shorter time scale (less than 65 days) the concentration of dissolved Sb(III) is significantly oversaturated with respect to this mineral phase, indicating that on this time scale sénarmontite precipitation is kinetically controlled. Similarly, the observed solubility of Sb(V) is higher than predicted by known solubility constants in systems containing Ca^{2+}. The aqueous concentration of Sb(V) is controlled by precipitation of mopungite ($NaSb(OH)_6$) in reactors where Na^+ exceeds 20 mM. The observed solubility of Sb(V) in the systems with Ca^{2+} and Pb^{2+} is several orders of magnitude larger than solubility reported for roméite and bindheimite (Diemar et al., 2009).

Second, the extent of Sb(III) oxidation to Sb(V) depends on the aqueous composition: Sb(V) is the predominant aqueous species (56–84% of total antimony) in the systems with simulated groundwater (SGW/Sb), dilute $NaNO_3$ (DI/Sb/$NaNO_3$) and $Ca(NO_3)_2$ (DI/Sb/$Ca(NO_3)_2$) solutions, and DI water (DI/Sb). Complexation with EDTA decreases the rate of Sb(III) oxidation to Sb(V), but does not stop this reaction. This might indicate that in berm soils with high organic matter content, Sb(III) will have a longer half-life compared to soils with low organic content.

Third, the addition of Pb(0) impedes the oxidation of Sb(0) to Sb(III) and further to Sb(V) due to either competitive oxidation, or to the coupling of antimony and lead redox reactions. Some Sb(0) remains in the systems after five months of reaction, as determined by XRD. These findings indicate that Pb(0) has a significant effect on the degree of Sb(0) oxidation and mobilization. During the corrosion of lead/antimony bullets, it is expected that the oxidation of Sb(0) will be inhibited prior to the complete oxidation of Pb(0).

These results show that simple solution components (Ca and Na), solution complexation and presence of Pb(0) are all significant factors controlling Sb(0) oxidation rates and pathways. Extension of these results to include more realistic soil/solution compositions (factoring in the role of iron, manganese and other common soil constituents) are needed to better understand and predict overall reactions in variable composition systems.

ACKNOWLEDGEMENTS

Funding of this project was provided by the U.S. Department of Defense's Strategic Environmental Research and development Program (SERDP) grant ER-1770. A portion of the work was funded by the U.S. Department of Energy, Office of Science, Office of Basic Energy Sciences. We thank Matt Newville for help with XAS data acquisition at GeoSoilEnviroCARS (Sector 13), Advanced Photon Source (APS), Argonne National Laboratory. Use of the Advanced Photon Source, an Office of Science User Facility operated for the U.S. Department of Energy (DOE) Office of Science by Argonne National Laboratory, is supported by the U.S. DOE under Contract No. DE-AC02-06CH11357. The GeoSoilEnviroCARS is supported by the National Science Foundation programs – Earth Sciences (EAR-1128799), and the Department of Energy, Geosciences (DE-FG02-94ER14466). Sandia National Laboratories is a multi-program laboratory managed and operated by Sandia Corporation, a wholly owned subsidiary of Lockheed Martin Corporation, for the U.S. Department of Energy's National Nuclear Security Administration under contract DE-AC04-94AL85000.

REFERENCES

Ackermann S., Gieré R., Newville M. and Majzlan J. (2009) Antimony sinks in the weathering crust of bullets from Swiss shooting ranges. *Sci. Total Environ.* **407**, 1669–1682.

Ashley P., Craw D., Graham B. and Chappell D. (2003) Environmental mobility of antimony around mesothermal stibnite deposits. New South Wales, Australia and southern New Zealand. *J. Geochem. Explor.* **77**, 1–14.

Basunia S. and Landsberger S. (2001) Contents and leachability of heavy metals (Pb, Cu, Sb, Zn, As) in soil at the Pantex firing range, Amarillo, Texas. *J. Air Waste Manage. Assoc.* **51**, 1428–1435.

Beauchemin S., John Kwong Y., Desbarats A. J., MacKinnon T., Percival J. B., Parsons M. B. and Pandya K. (2012) Downstream changes in antimony and arsenic speciation in sediments at a mesothermal gold deposit in British Columbia, Canada. *Appl. Geochem.* **27**, 1953–1965.

Belzile N., Chen Y. and Wang Z. (2001) Oxidation of antimony (III) by amorphous iron and manganese oxyhydroxides. *Chem. Geol.* **174**, 379–387.

Bethke C. (1998) *The geochemist's workbench release 8.0*. University of Illinois at Urbana-Champaign, Champaign, IL.

Beyersmann D. and Hartwig A. (2008) Carcinogenic metal compounds: recent insight into molecular and cellular mechanisms. *Arch. Toxicol.* **82**, 493–512.

Blandamer M. J., Peacock R. D. and Burgess J. (1974) Solubility of sodium hexahydroxoantimonate in water and in mixed aqueous solvents. *J. Chem. Soc., Dalton Trans.*, 1084–1086.

Carlin Jr J. (2012) Antimony, U.S. geological survey, mineral commodity summaries. <http://minerals.usgs.gov/minerals/pubs/mcs/2012/mcs2012.pdf> (accessed 1/2/2013).

Chung F. H. (1974a) A Quantitative interpretation of X-ray diffraction patterns of mixtures. I. Matrix-flushing method for quantitative multicomponent analysis. *J. Appl. Crystallogr.* **7**, 519–525.

Chung F. H. (1974b) B Quantitative interpretation of X-ray diffraction patterns of mixtures. II. Adiabatic principle of X-ray diffraction analysis of mixtures. *J. Appl. Crystallogr.* **7**, 526–531.

Chung F. H. (1975) Quantitative interpretation of X-ray diffraction patterns of mixtures. III. Simultaneous determination of a set of reference intensities. *J. Appl. Crystallogr.* **8**, 17–19.

Diemar G. A., Filella M., Leverett P. and Williams P. A. (2009) Dispersion of antimony from oxidizing ore deposits. *Pure Appl. Chem.* **81**(9), 1547–1553.

Elleouet C., Quentel F., Madec C. L. and Filella M. (2005) The effect of the presence of trace metals on the oxidation of Sb (III) by hydrogen peroxide in aqueous solution. *J. Environ. Monit.* **7**, 1220–1225.

Ettler V., Mihaljevič M., Šebek O. and Nechutný Z. (2007) Antimony availability in highly polluted soils and sediments–a comparison of single extractions. *Chemosphere* **68**, 455–463.

Filella M., Belzile N. and Chen Y. (2002) Antimony in the environment: a review focused on natural waters I. Occurrence. *Earth-Sci. Rev.* **57**, 125–176.

Filella M. and May P. M. (2005) Critical appraisal of available thermodynamic data for the complexation of antimony (III) and antimony (V) by low molecular mass organic ligands. *J. Environ. Monit.* **7**, 1226–1237.

Filella M., Williams P. and Belzile N. (2009) Antimony in the environment: knowns and unknowns. *Environ. Chem.* **6**, 95–105.

Filella M. and Williams P. A. (2012) Antimony interactions with heterogeneous complexants in waters, sediments and soils: a review of binding data for homologous compounds. *Chem. Erde* **72**(4), 49–65.

Gebel T. (1997) Arsenic and antimony: comparative approach on mechanistic toxicology. *Chem. Biol. Interact.* **107**, 131–144.

Heier L. S., Meland S., Ljønes M., Salbu B. and Strømseng A. E. (2010) Short-term temporal variations in speciation of Pb, Cu, Zn and Sb in a shooting range runoff stream. *Sci. Total Environ.* **408**(11), 2409–2417.

Ilgen A., Foster A. and Trainor T. (2012) Role of structural Fe in nontronite NAu-1 and dissolved Fe(II) in redox transformations of arsenic and antimony. *Geochim. Cosmochim. Acta* **94**, 128–145.

Ilgen A. and Trainor T. (2012) Sb(III) and Sb(V) sorption onto Al-rich phases: hydrous Al oxide and the clay minerals kaolinite KGa-1b and oxidized and reduced nontronite NAu-1. *Environ. Sci. Technol.* **46**, 843–851.

Johnson C., Moench H., Wersin P., Kugler P. and Wenger C. (2005) Solubility of antimony and other elements in samples taken from shooting ranges. *J. Environ. Qual.* **34**, 248.

Kelly S., Hesterberg D. and Ravel B. (2008) Analysis of soils and minerals using X-ray absorption spectroscopy. In *Methods of Soil Analysis: Part 5–Mineralogical Methods* (eds. A. Ulery and L. Drees). Soil Science Society of America, Inc., Madison, WI, USA, p. 387.

Keto R. O. (1999) Analysis and comparison of bullet leads by inductively-coupled plasma mass spectrometry. *J. Forensic Sci.* **44**, 1020–1026.

Knechtenhofer L. A., Xifra I. O., Scheinost A. C., Flühler H. and Kretzschmar R. (2003) Fate of heavy metals in a strongly acidic shooting-range soil: small-scale metal distribution and its relation to preferential water flow. *J. Plant Nutr. Soil Sci.* **166**, 84–92.

Léonard A. and Gerber G. (1996) Mutagenicity, carcinogenicity and teratogenicity of antimony compounds. *Mutat. Res. Rev. Genet. Toxicol.* **366**, 1–8.

Leuz A., Hug S., Wehrli B. and Johnson C. (2006a) Iron-mediated oxidation of antimony (III) by oxygen and hydrogen peroxide compared to arsenic (III) oxidation. *Environ. Sci. Technol.* **40**, 2565–2571.

Leuz A. and Johnson C. (2005) Oxidation of Sb (III) to Sb (V) by O_2 and H_2O_2 in aqueous solutions. *Geochim. Cosmochim. Acta* **69**, 1165–1172.

Leuz A., Mönch H. and Johnson C. (2006b) Sorption of Sb (III) and Sb (V) to goethite: influence on Sb (III) oxidation and mobilization. *Environ. Sci. Technol.* **40**, 7277–7282.

Lide D. (1993) *CRC Handbook of Chemistry and Physics*, 72 ed. CRC Press.

Linarez Pérez O. E., Sánchez M. D. and López Teijelo M. (2010) Characterization of growth of anodic antimony oxide films by ellipsometry and XPS. *J. Electroanal. Chem.* **645**, 143–148.

Liu F., Le X. C., McKnight-Whitford A., Xia Y., Wu F., Elswick E., Johnson C. C. and Zhu C. (2010) Antimony speciation and contamination of waters in the Xikuangshan antimony mining and smelting area, China. *Environ. Geochem. Health* **32**, 401–413.

Martell A. and Smith R. (1974) *Critical Stability Constants*. Plenum, New York.

Newville M. (2001) IFEFFIT: interactive XAFS analysis and FEFF fitting. *J. Synch. Radiat.* **8**, 322–324.

Newville M., Livins P., Yacoby Y., Rehr J. and Stern E. (1993) Near-edge x-ray-absorption fine structure of Pb: a comparison of theory and experiment. *Phys. Rev. B Condens. Matter Mater. Phys.* **47**, 14126–14131.

Olivé I. (2006) Mobility of lead and antimony in shooting range soils. Ph. D. thesis, Swiss Federal Institute of Technology Zurich.

Pilarski J., Waller P. and Pickering W. (1995) Sorption of antimony species by humic acid. *Water Air Soil Pollut.* **84**, 51–59.

Rakshit S., Sarkar D., Punamiya P. and Datta R. (2011) Antimony sorption at gibbsite–water interface. *Chemosphere* **84**(4), 480–483.

Randich E., Duerfeldt W., McLendon W. and Tobin W. (2002) A metallurgical review of the interpretation of bullet lead compositional analysis. *Forensic Sci. Int.* **127**, 174–191.

Ravel B. and Newville M. (2005) ATHENA, ARTEMIS, HEPHAESTUS: data analysis for X-ray absorption spectroscopy using IFEFFIT. *J. Synch. Radiat.* **12**, 537–541.

Reimann C., Matschullat J., Birke M. and Salminen R. (2010) Antimony in the environment: lessons from geochemical mapping. *Appl. Geochem.* **25**, 175–198.

Ritchie V. J., Ilgen A. G., Mueller S. H., Trainor T. P. and Goldfarb R. J. (2013) Mobility and chemical fate of antimony and arsenic in historic mining environments of the Kantishna Hills district, Denali National Park and Preserve, Alaska. *Chem. Geol.* **335**, 172–188.

Roper A. J., Williams P. A. and Filella M. (2012) Secondary antimony minerals: phases that control the dispersion of antimony in the supergene zone. *Chem. Erde* **72**(4), 9–14.

Scheinost A., Rossberg A., Vantelon D., Xifra I., Kretzschmar R., Leuz A., Funke H. and Johnson C. (2006) Quantitative antimony speciation in shooting-range soils by EXAFS spectroscopy. *Geochim. Cosmochim. Acta* **70**, 3299–3312.

Snyder R. L. (1992) The use of reference intensity ratios in X-ray quantitative analysis. *Powder Diffr.* **7**(4), 186–193.

Strømseng A. E., Ljønes M., Bakka L. and Mariussen E. (2009) Episodic discharge of lead, copper and antimony from a Norwegian small arm shooting range. *J. Environ. Monit.* **11**, 1259–1267.

Thanabalasingam P. and Pickering W. (1990) Specific sorption of antimony (III) by the hydrous oxides of Mn, Fe, and Al. *Water Air Soil Pollut.* **49**, 175–185.

Tighe M., Lockwood P. and Wilson S. (2005) Adsorption of antimony (V) by floodplain soils, amorphous iron (III) hydroxide and humic acid. *J. Environ. Monit.* **7**, 1177–1185.

US EPA Report EPA-902-B-01-001. (2005) Best management practices for lead at outdoor shooting ranges.

Whitten A., Dittrich B., Spackman M., Turner P. and Brown T. (2004) Charge density analysis of two polymorphs of antimony (III) oxide. *Dalton Trans.* **1**, 23–29.

Wilson S., Lockwood P., Ashley P. and Tighe M. (2010) The chemistry and behaviour of antimony in the soil environment with comparisons to arsenic: a critical review. *Environ. Pollut.* **158**, 1169–1181.

Wyckoff R. W. G. (1963). .

Xi J., He M. and Lin C. (2010) Adsorption of antimony (V) on kaolinite as a function of pH, ionic strength and humic acid. *Environ. Earth Sci.* **60**, 715–722.

Xi J., He M. and Lin C. (2011) Adsorption of antimony (III) and antimony (V) on bentonite: kinetics, thermodynamics and anion competition. *Microchem. J.* **97**, 85–91.

Xu W., Wang H., Liu R., Zhao X. and Qu J. (2011) The mechanism of antimony (III) removal and its reactions on the surfaces of Fe–Mn binary oxide. *J. Colloid Interface Sci.* **363**(1), 320–326.

Zabinsky S., Rehr J., Ankudinov A., Albers R. and Eller M. (1995) Multiple-scattering calculations of x-ray-absorption spectra. *Phys. Rev. B Condens. Matter Mater. Phys.* **52**, 2995–3009.

Zheng J., Iijima A. and Furuta N. (2001) Complexation effect of antimony compounds with citric acid and its application to the speciation of antimony (III) and antimony (V) using HPLC-ICP-MS. *J. Anal. At. Spectrom.* **16**, 812–818.

Zotov A., Shikina N. and Akinfiev N. (2003) Thermodynamic properties of the Sb (III) hydroxide complex Sb (OH) 3 (aq) at hydrothermal conditions. *Geochim. Cosmochim. Acta* **67**, 1821–1836.

Associate editor: Karen Johannesson